Progress In Electromagnetics Research, Vol. 127, 155–171, 2012

ANALYTICAL FIELD CALCULATION FOR LINEAR TUBULAR MAGNETIC GEARS USING EQUIVALENT ANISOTROPIC MAGNETIC PERMEABILITY

W. Li and K. T. Chau*

Department of Electrical and Electronic Engineering, The University of Hong Kong, Pokfulam Road, Hong Kong, China

Abstract—Linear magnetic gears take the definite merit of direct force amplification or speed reduction without using any bulky, inefficient rotary-to-linear mechanism. In this paper, an analytical calculation approach to determine the performance of linear tubular magnetic gears is proposed. The key is to adopt the concept of anisotropic magnetic permeability to handle the field-modulation region which consists of iron rings and airspaces in a zebra-striped manner. By solving the Laplace's and Poisson's equations in the linear tubular magnetic gear, the corresponding magnetic field distributions can be analytically determined. Finally, the analytical calculation results are compared with the numerical results obtained from the finite element method, hence verifying the validity of the proposed analytical field calculation.

1. INTRODUCTION

There is no doubt that mechanical gears were one of the most important inventions, which can scale up and down the torque and speed to satisfy various application needs. With ever increasing demand on the transmission efficiency and reliability, mechanical gears are being challenged by a new class of transmission devices — magnetic gears. These magnetic gears employ magnetic attraction for torque transmission, hence eliminating the transmission loss and wear-and-tear problem [1, 2]. Moreover, the magnetic gears can readily be integrated into the permanent magnet (PM) machines to form a special class of PM machines — the magnetic-geared PM machines. They can enable high-speed rotating-field design to increase the torque

Received 3 March 2012, Accepted 27 March 2012, Scheduled 11 April 2012

* Corresponding author: Kwok Tong Chau (ktchau@eee.hku.hk).

density while offering low-speed output rotation for in-wheel direct-drive electric vehicles [3]. Also, they can perform online power splitting of the engine power for electric variable transmission, hence offering the optimal operation line for hybrid electric vehicles [4].

In order to handle linear motion, both the mechanical gears and magnetic gears generally need to couple with a rotary-to-linear mechanism which is bulky, heavy and inefficient. In recent years, the concept of magnetic gears has been extended to the linear morphology, namely the linear tubular magnetic gear as shown in Figure 1 [5, 6]. With the use of linear magnetic gears, the linear motion can be directly handled without using any rotary-to-linear mechanism, such as the linear free-piston generator for range-extended electric vehicles [7] and the linear generator for wave energy harvesting [8].

In order to design and analyze the magnetic gear performances, the finite element method (FEM) has been widely adopted [9–11]. The finite element method is an excellent tool for numerical field calculation, but it provides little information on the relationship of the machine geometry and its performance, and usually needs lengthy computation [11]. To complement the FEM, the analytical calculation for field analysis of machines including magnetic gears is highly desirable [12–14]. However, the available analytical calculation method for magnetic gears is developed for the coaxial topology [12]. Also, because each airspace in the corresponding field-modulation region needs to be modeled separately, the resulting analytical expression is very complicated.

The purpose of this paper is to propose an analytical calculation method for linear tubular magnetic gears. The key is to adopt the

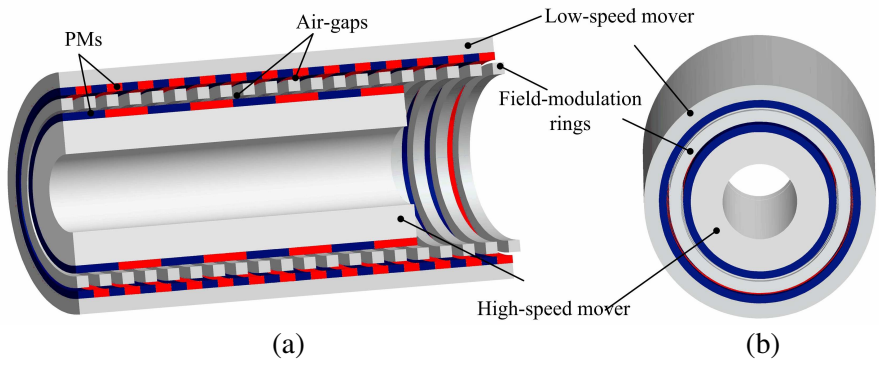

Figure 1. Linear tubular magnetic gear. (a) Front view. (b) Side view.

concept of anisotropic magnetic permeability to model the whole field-modulation region, rather than to handle each airspace separately. Firstly, the linear tubular magnetic gear will be analytically modeled. Then, the corresponding magnetic field solution will be derived. Consequently, the magnetic field distributions will be calculated by using the proposed approach, and finally verified by comparing with the FEM results.

2. ANALYTICAL MODEL

In the linear tubular magnetic gear, the magnetic fields are only produced by PMs and no current source is involved. Thus the magnetic scalar potential ψ is adopted for the magnetic field calculation. In order to facilitate the analytical modeling, the following assumptions are made:

(1) The permeability of back irons of two movers is assumed to be infinite.

(2) The relative recoil permeability of PMs is assumed to be linear.

(3) The axial length is infinite so that the field distribution is axially symmetric and periodic.

(4) The field-modulation region is considered to be composed of anisotropic magnetic material in which the permeabilities along the r-direction and the z-direction are different.

Figure 2 shows the model of the linear tubular magnetic gear. The field-modulation region consists of field-modulation rings and airspaces interleaving one another. From the point of view of the magnetic circuit, it can be decomposed into the r and z directions. Namely, in the r-direction, the field-modulation ring reluctance R_{fm} and airspace reluctance R_{as} are connected in parallel, whereas in the z-direction, the two reluctance are connected in series. Therefore, the permeabilities along the two directions can be expressed as:

$$\mu_{fm\_r} = \mu_0 \left(1 - \frac{b_t}{\tau_t}\right) + \mu_{ic} \frac{b_t}{\tau_t} \tag{1}$$

$$\mu_{fm\_z} = \frac{\mu_0 \mu_{ic} \tau_t}{\mu_{ic} \tau_t + b_t(\mu_0 - \mu_{ic})} \tag{2}$$

where μ_0 is the airspace permeability, μ_{ic} is the iron core permeability, b_t is the width of the field-modulation rings, and τ_t is the pole-pitch of the field-modulation ring.

In order to ease the modeling, PMs on the high-speed mover and the low-speed mover are handled individually. Then, by using the superposition law, the resultant magnetic field distribution can be

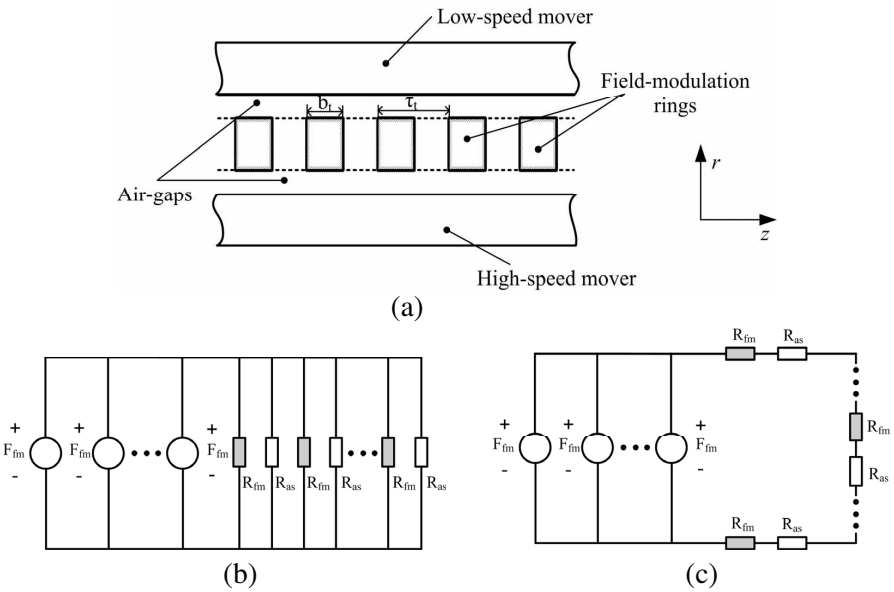

Figure 2. Linear tubular magnetic gear model. (a) Schematic diagram. (b) Equivalent magnetic circuit of field-modulation region along r-direction. (c) Equivalent magnetic circuit of field-modulation region along z-direction.

obtained. Firstly, PMs on the high-speed mover are considered while PMs on the low-speed mover are considered as airspace. Taking the above-mentioned assumptions, the calculation areas can be divided into four regions, namely the high-speed mover PM region I, the inner air-gap region II, the field-modulation region III, and the outer airspace region IV, as shown in Figure 3. The field density $\bar{B}$ and field intensity $\bar{H}$ in each region can be deduced accordingly.

In region I, where PMs are involved, it yields:

$$\bar{B} = \mu_0 \left(\mu_{rm}\bar{H} + \bar{M}\right) \tag{3}$$

where μ_{rm} is the relative recoil permeability of PMs, and $\bar{M}$ is the residual magnetization vector.

In region III, where the material is anisotropic along the r and z directions, it yields:

$$\bar{B}_r = \mu_{fm\_r}\bar{H}_r \tag{4}$$

$$\bar{B}_z = \mu_{fm\_z}\bar{H}_z \tag{5}$$

In regions II and IV, they are simply governed by:

$$\bar{B} = \mu_0\bar{H} \tag{6}$$

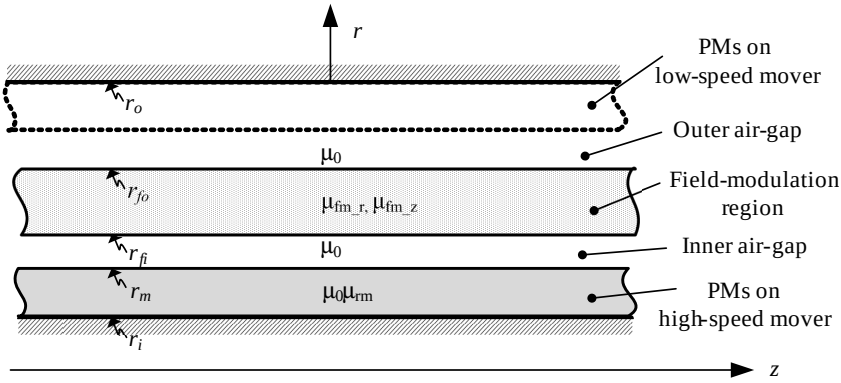

Figure 3. Field regions and boundaries.

Due to the symmetry of the tubular structure, the 3-D problem can be reduced to a 2-D problem in which only the radial and axial components exist. The governing field equations in the four regions can be derived by using the Laplace's and Poisson's equations accordingly.

In region I, the governing equation can be expressed as:

$$\frac{\partial^2 \psi^{\mathrm{I}}}{\partial r^2} + \frac{1}{r}\frac{\partial \psi^{\mathrm{I}}}{\partial r} + \frac{\partial^2 \psi^{\mathrm{I}}}{\partial z^2} = \frac{1}{r\mu_{rm}}\frac{\partial}{\partial r}(rM_r) \tag{7}$$

where M_r is the radial component of the residual magnetization vector.

In regions II and IV, the governing equation can be written as:

$$\frac{\partial^2 \psi^{\mathrm{II,IV}}}{\partial r^2} + \frac{1}{r}\frac{\partial \psi^{\mathrm{II,IV}}}{\partial r} + \frac{\partial^2 \psi^{\mathrm{II,IV}}}{\partial z^2} = 0 \tag{8}$$

In region III, the governing equation can be deduced as:

$$\mu_{fm\_r}\left(\frac{\partial^2 \psi^{\mathrm{III}}}{\partial r^2} + \frac{1}{r}\frac{\partial \psi^{\mathrm{III}}}{\partial r}\right) + \mu_{fm\_z}\frac{\partial^2 \psi^{\mathrm{III}}}{\partial z^2} = 0 \tag{9}$$

In order to solve the above equations, the boundary conditions need to be identified. As shown in Figure 3, there are five boundaries formed by the four regions where r_i, r_m, r_{fi}, r_{fo} and r_o are the radii of the high-speed mover yoke, the surface of PMs on the high-speed mover, the inner surface of the field-modulation region, the outer surface of the field-modulation region and the low-speed mover yoke respectively.

When $r = r_i$, it yields:

$$H_z^{\mathrm{I}}(r_i, z) = 0 \tag{10}$$

When $r = r_m$, it yields:

$$H_z^{\mathrm{I}}(r_m, z) = H_z^{\mathrm{II}}(r_m, z) \tag{11}$$

$$B_r^{\mathrm{I}}(r_m, z) = B_r^{\mathrm{II}}(r_m, z) \tag{12}$$

When $r = r_{fi}$, it yields:

$$H_z^{\mathrm{II}}(r_{fi}, z) = H_z^{\mathrm{III}}(r_{fi}, z) \tag{13}$$

$$B_r^{\mathrm{II}}(r_{fi}, z) = B_r^{\mathrm{III}}(r_{fi}, z) \tag{14}$$

When $r = r_{fo}$, it yields:

$$H_z^{\mathrm{III}}(r_{fo}, z) = H_z^{\mathrm{IV}}(r_{fo}, z) \tag{15}$$

$$B_r^{\mathrm{III}}(r_{fo}, z) = B_r^{\mathrm{IV}}(r_{fo}, z) \tag{16}$$

When $r = r_o$, it yields:

$$H_z^{\mathrm{IV}}(r_o, z) = 0 \tag{17}$$

It should be noted that since the axial length of the linear tubular magnetic gear is assumed to be infinite, all the boundary conditions are only radially dependent.

3. MAGNETIC FIELD SOLUTION

By using the separation of variables, the magnetic field equations in regions II, III and IV governed by the Laplace's equation can be decomposed into a Helmholtz equation and a Bessel equation. Then, by solving the two equations, a general solution can be obtained.

3.1. Field Solution in Regions without PMs

In region II, the solution of ψ can be expressed as:

$$\psi^{\mathrm{II}} = \sum_{n=1}^{+\infty} \left[a_n^{\mathrm{II}} I_0(k_n r) + b_n^{\mathrm{II}} K_0(k_n r)\right] \times \left[c_n^{\mathrm{II}} \sin(k_n z) + d_n^{\mathrm{II}} \cos(k_n z)\right] \tag{18}$$

where $I_0(\cdot)$ and $K_0(\cdot)$ are the modified Bessel functions of the first kind and the second kind of order zero, respectively.

In region III, the solution of ψ can be written as:

$$\psi^{\mathrm{III}} = \sum_{n=1}^{+\infty} \left[a_n^{\mathrm{III}} I_0(p_n r) + b_n^{\mathrm{III}} K_0(p_n r)\right] \times \left[c_n^{\mathrm{III}} \sin(k_n z) + d_n^{\mathrm{III}} \cos(k_n z)\right] \tag{19}$$

where

$$p_n = \frac{\sqrt{\mu_{fm\_z}}}{\sqrt{\mu_{fm\_r}}} k_n \tag{20}$$

In region IV, the solution of ψ can be deduced as:

$$\begin{aligned} \psi^{\mathrm{IV}} &= \sum_{n=1}^{+\infty} \left[a_n^{\mathrm{IV}} I_0(k_n r) + b_n^{IV} K_0(k_n r) \right] \\ &\quad \times \left[c_n^{\mathrm{IV}} \sin(k_n z) + d_n^{\mathrm{IV}} \cos(k_n z) \right] \end{aligned} \tag{21}$$

3.2. Field Solution in Region with PMs

For region I, the magnetic field equation is governed by the Poisson's equation. Its solution consists of a general solution and a particular solution. The general solution has the same form as the other three regions:

$$\psi_o^{\mathrm{I}} = \sum_{n=1}^{+\infty} \left[a_n^{\mathrm{I}} I_0(k_n r) + b_n^{\mathrm{I}} K_0(k_n r) \right] \times \left[c_n^{\mathrm{I}} \sin(k_n z) + d_n^{\mathrm{I}} \cos(k_n z) \right] \tag{22}$$

The special solution depends on the magnetization distribution of PMs. Figure 4 depicts the PM magnetization distribution M_r on the high-speed mover. Since the PMs are radially magnetized, the magnetization function is only z-dependent. In general, it can be expressed as [14]:

$$M_r = \frac{R_1 \left(R_2 + r^2 \right)}{r} \sum_{n=1}^{+\infty} M_n \sin(\omega_n z) \tag{23}$$

where

$$R_1 = \frac{1}{r_i + r_m} \tag{24}$$

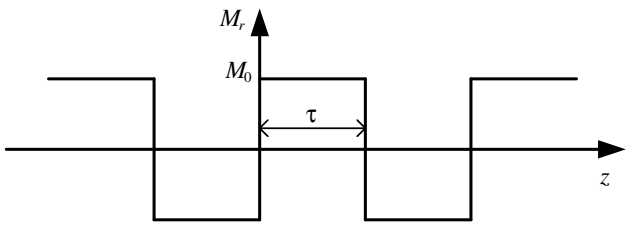

Figure 4. PM magnetization distribution.

$$R_2 = r_i r_m \tag{25}$$

$$\omega_n = \frac{2n-1}{\tau}\pi \tag{26}$$

$$M_n = \frac{4B_{res}}{\mu_0}\frac{1}{(2n-1)\pi} \tag{27}$$

where r_i and r_m are the radii of the high-speed mover and the PMs on the high-speed mover respectively, and B_{res} is the residual flux density of PMs. Thus, by using the separation of variables, the particular solution can be deduced as:

$$\psi_p^{\mathrm{I}} = -\frac{2R_1}{\mu_{rm}}\sum_{n=1}^{+\infty}\frac{M_n}{\omega_n^2}\sin(\omega_n z) = -2R_0\sum_{n=1}^{+\infty}\frac{M_n}{\omega_n^2}\sin(\omega_n z) \tag{28}$$

3.3. Boundary Conditions

Based on the boundary conditions of each region, the coefficients of the above equations can be determined accordingly.

Firstly, on the surface of the high-speed mover back iron, from (10), it yields:

$$\left[A_n^{\mathrm{I}} I_0(k_n r_i) + B_n^{\mathrm{I}} K_0(k_n r_i)\right]\cos(k_n z) - 2R_0\frac{M_n}{\omega_n^2}\cos(\omega_n z) = 0 \tag{29}$$

Thus, it further yields:

$$k_n = \omega_n \tag{30}$$

$$A_n^{\mathrm{I}} = \frac{2R_0 M_n}{I_0(\omega_n r_i)\omega_n^2} - F(\omega_n, \omega_n, r_i, 0)B_n^{\mathrm{I}} \tag{31}$$

Secondly, on the surface of the low-speed mover back iron, from (17), it yields:

$$A_n^{\mathrm{IV}} I_0(\omega_n r_o) + B_n^{\mathrm{IV}} K_0(\omega_n r_o) = 0 \tag{32}$$

Thirdly, on the surface of the PMs on the high-speed mover, from (11) and (12), it yields:

$$\begin{aligned} & A_n^{\mathrm{I}} I_0(\omega_n r_m) + B_n^{\mathrm{I}} K_0(\omega_n r_m) - 2R_0\frac{M_n}{\omega_n^2} \\ = \; & A_n^{\mathrm{II}} I_0(\omega_n r_m) + B_n^{\mathrm{II}} K_0(\omega_n r_m) \end{aligned} \tag{33}$$

$$\begin{aligned} & \mu_{rm}[A_n^{\mathrm{I}} I_1(\omega_n r_m) - B_n^{\mathrm{I}} K_1(\omega_n r_m)] + \frac{M_n}{\omega_n} \\ = \; & A_n^{\mathrm{II}} I_1(\omega_n r_m) - B_n^{\mathrm{II}} K_1(\omega_n r_m) \end{aligned} \tag{34}$$

where $I_1(\cdot)$ and $K_1(\cdot)$ are the modified Bessel functions of the first kind and the second kind of order one, respectively.

Fourthly, on the inner surface of the field-modulation region, from (13) and (14), it yields:

$$\begin{aligned} & A_n^{\mathrm{II}} I_0(\omega_n r_{fi}) + B_n^{\mathrm{II}} K_0(\omega_n r_{fi}) \\ = \; & A_n^{\mathrm{III}} I_0(p_n r_{fi}) + B_n^{\mathrm{III}} K_0(p_n r_{fi}) \end{aligned} \tag{35}$$

$$\begin{aligned} & \mu_0 \omega_n \left[A_n^{\mathrm{II}} I_1(\omega_n r_{fi}) - B_n^{\mathrm{II}} K_1(\omega_n r_{fi}) \right] \\ = \; & \mu_{fm\_r} p_n \left[A_n^{\mathrm{III}} I_1(p_n r_{fi}) - B_n^{\mathrm{III}} K_1(p_n r_{fi}) \right] \end{aligned} \tag{36}$$

Finally, on the outer surface of the field-modulation region, from (15) and (16), it yields:

$$\begin{aligned} & A_n^{\mathrm{III}} I_0(p_n r_{fo}) + B_n^{\mathrm{III}} K_0(p_n r_{fo}) \\ = \; & A_n^{\mathrm{IV}} I_0(\omega_n r_{fo}) + B_n^{\mathrm{IV}} K_0(\omega_n r_{fo}) \end{aligned} \tag{37}$$

$$\begin{aligned} & \mu_{fm\_r} p_n [A_n^{\mathrm{III}} I_1(p_n r_{fo}) - B_n^{\mathrm{III}} K_1(p_n r_{fo})] \\ = \; & \mu_0 \omega_n \left[A_n^{\mathrm{IV}} I_1(\omega_n r_{fo}) - B_n^{\mathrm{IV}} K_1(\omega_n r_{fo}) \right] \end{aligned} \tag{38}$$

By solving (29)–(38), the coefficients can be determined. The corresponding details are given in the Appendix. With these solutions, the magnetic scalar potential expression in each region can be expressed in a Fourier series. Namely, in the inner air-gap, it is given by:

$$\psi^{\mathrm{II}} = \sum_{n=1}^{+\infty} \left[A_n^{\mathrm{II}} I_0(\omega_n r) + B_n^{\mathrm{II}} K_0(\omega_n r) \right] \times \sin(\omega_n z) \tag{39}$$

Meanwhile, in the outer air-gap, it is given by:

$$\psi^{\mathrm{IV}} = \sum_{n=1}^{+\infty} \left[A_n^{\mathrm{IV}} I_0(\omega_n r) + B_n^{\mathrm{IV}} K_0(\omega_n r) \right] \times \sin(\omega_n z) \tag{40}$$

where A_n^{II}, B_n^{II}, A_n^{IV}, and B_n^{IV} are the coefficients determined by the boundary conditions which are given in Appendix A.

4. CALCULATION RESULTS AND VERIFICATION

In order to verify the proposed calculation, a practical linear tubular magnetic gear is adopted for exemplification. Table 1 lists its key data.

According to (39) and (40), the magnetic scalar potential distributions at both the inner and outer air-gaps can be calculated as shown in Figure 5 in which the effects due to PMs on the high-speed and low-speed movers are determined separately. In order to determine the performance of the linear tubular magnetic gear, the magnetic flux density distributions at the inner and outer air-gaps can be deduced from the corresponding magnetic scalar potential distributions.

Table 1. Key data of linear tubular magnetic gear.

High-speed mover yoke radius	16 mm
High-speed mover PM pole-pitch	12 mm
Low-speed mover PM pole-pitch	6 mm
PM height	4 mm
Air-gap length	1 mm
Field-modulation ring height	6 mm
Field-modulation ring width	4 mm
Field-modulation ring pitch	8 mm
Field-modulation ring relative permeability	4000
PM relative permeability	1.09
PM remanence	1.23 T
PM coercivity	890 kA/m

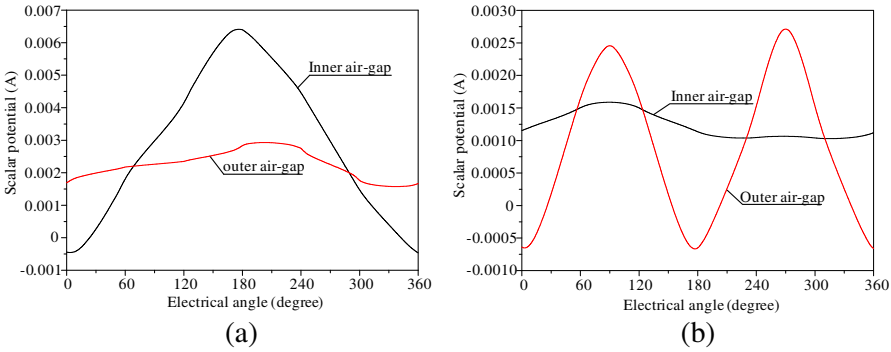

Figure 5. Magnetic scalar potentials at inner and outer air-gaps. (a) Due to PMs on high-speed mover. (b) Due to PMs on low-speed mover.

Firstly, when the PMs on the high-speed mover are considered while those on the low-speed mover are ignored, the magnetic flux density distributions in the inner air-gap are given by:

$$B_r^{\mathrm{II}} = \mu_0 \sum_{n=1}^{+\infty} \omega_n \left[-A_n^{\mathrm{II}} I_1(\omega_n r) + B_n^{\mathrm{II}} K_1(\omega_n r) \right] \times \sin(\omega_n z) \tag{41}$$

$$B_z^{\mathrm{II}} = -\mu_0 \sum_{n=1}^{+\infty} \omega_n \left[A_n^{\mathrm{II}} I_0(\omega_n r) + B_n^{\mathrm{II}} K_0(\omega_n r) \right] \times \cos(\omega_n z) \tag{42}$$

Similarly, the magnetic flux density distributions in the outer air-gap

are given by:

$$B_r^{\mathrm{IV}} = \mu_0 \sum_{n=1}^{+\infty} \omega_n \left[-A_n^{\mathrm{IV}} I_1(\omega_n r) + B_n^{\mathrm{IV}} K_1(\omega_n r) \right] \times \sin(\omega_n z) \quad (43)$$

$$B_z^{\mathrm{IV}} = -\mu_0 \sum_{n=1}^{+\infty} \omega_n \left[A_n^{\mathrm{IV}} I_0(\omega_n r) + B_n^{\mathrm{IV}} K_0(\omega_n r) \right] \times \cos(\omega_n z) \quad (44)$$

Consequently, the corresponding air-gap flux density distributions are calculated as depicted in Figure 6 in which the radial and tangential components are separately plotted. In order to verify the analytical calculation, the air-gap flux density distributions are also numerically computed by using the FEM. By comparing the analytical results with the FEM results, it can verify that the proposed analytical calculation

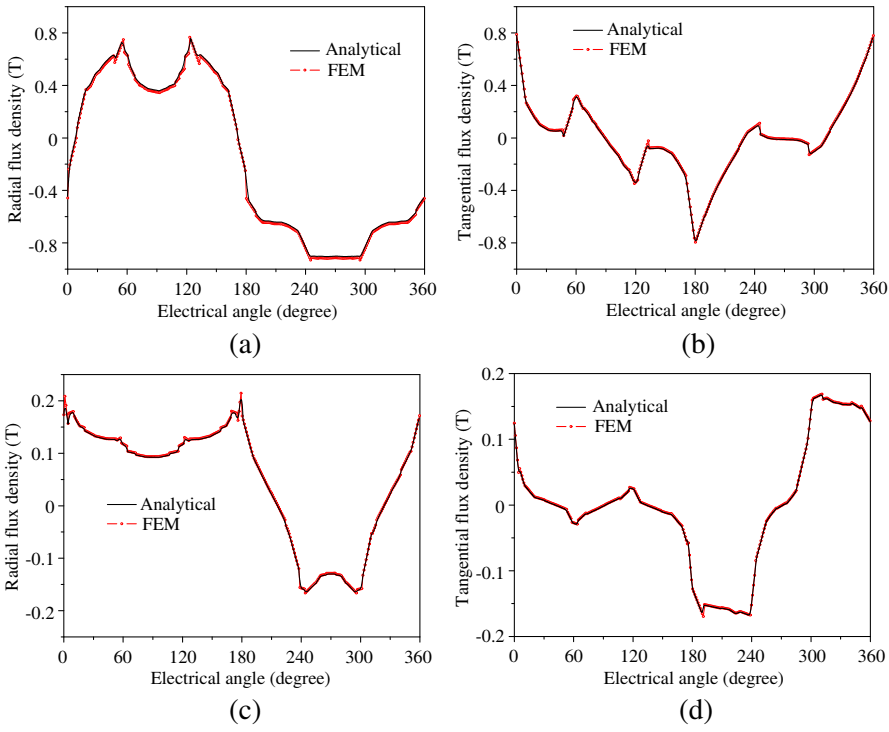

Figure 6. Magnetic flux density distributions due to PMs on high-speed mover. (a) Radial component in inner air-gap. (b) Tangential component in inner air-gap. (c) Radial component in outer air-gap. (d) Tangential component in outer air-gap.

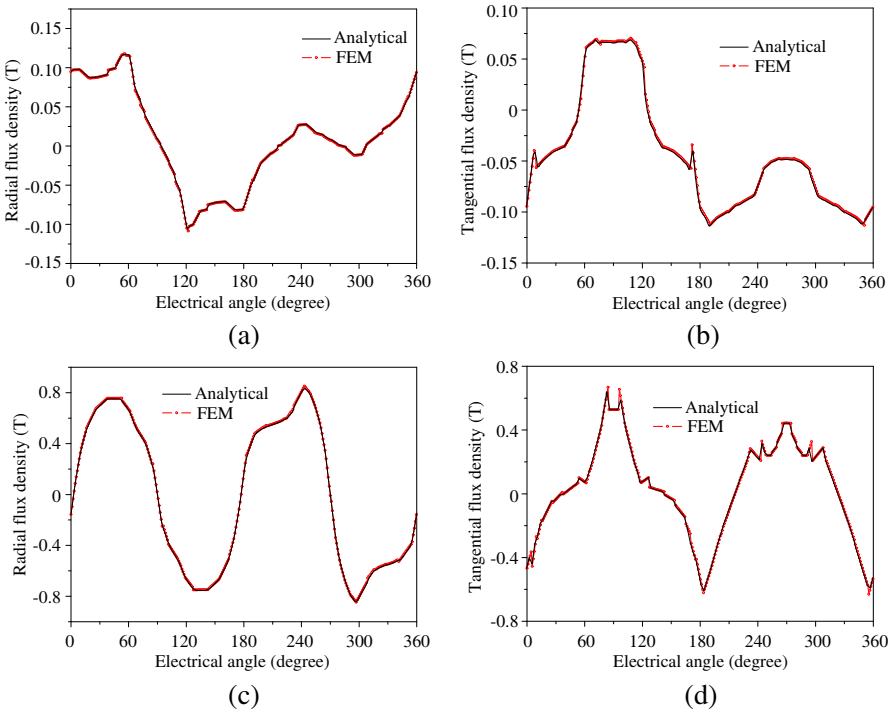

Figure 7. Magnetic flux density distributions due to PMs on low-speed mover. (a) Radial component in inner air-gap. (b) Tangential component in inner air-gap. (c) Radial component in outer air-gap. (d) Tangential component in outer air-gap.

can provide the same level of accuracy as the FEM. It should be noted that the analytical calculation takes the definite advantages that it can provide insight of the relationship between the machine geometry and its performance, and can avoid lengthy computation for design optimization.

Secondly, when the PMs on the high-speed mover are ignored while that on the low-speed mover are considered, the corresponding air-gap flux density distributions are calculated as depicted in Figure 7 which are obtained based on the same approach. Again, by comparing the analytical results with the FEM results, it can further verify that the proposed analytical calculation can provide the same level of accuracy as the FEM.

Finally, by applying the superposition law, the analytically calculated magnetic flux density distributions in the two air-gaps due

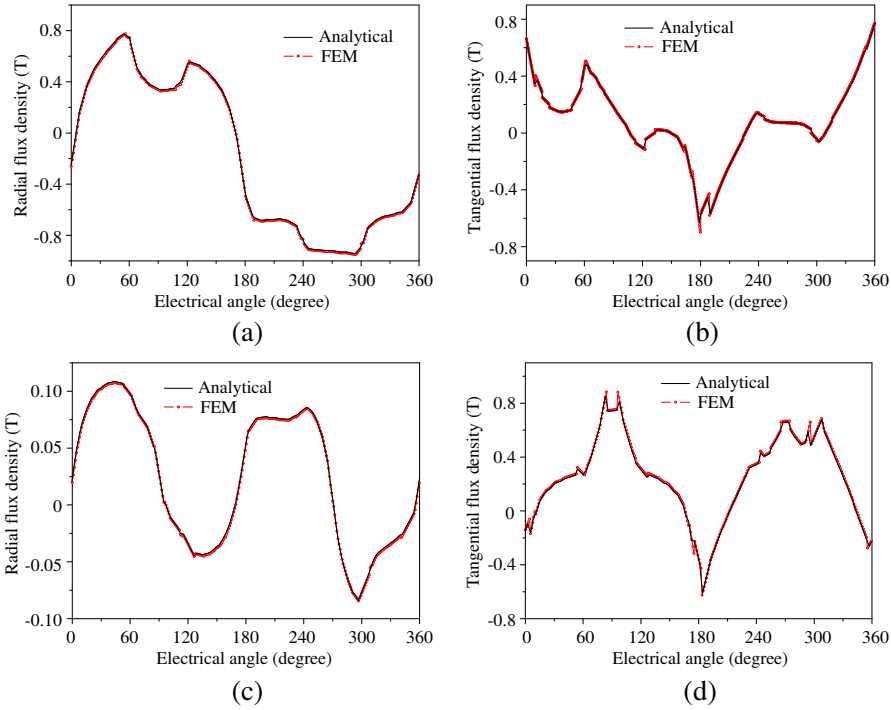

Figure 8. Magnetic flux density distributions due to PMs on both movers. (a) Radial component in inner air-gap. (b) Tangential component in inner air-gap. (c) Radial component in outer air-gap. (d) Tangential component in outer air-gap.

to PMs on both movers can be deduced from Figures 6 and 7. As shown in Figure 8, the analytical distributions are well verified by comparison with the numerical distributions obtained from using the FEM.

5. CONCLUSIONS

In this paper, an analytical approach for calculation of magnetic field distributions in linear tubular magnetic gears has been proposed. Compared with conventional analytical approaches, the concept of anisotropic magnetic permeability is firstly utilized to model the field-modulation region. Thus the proposed analytical expression can be much simplified and the analytical calculation can be greatly reduced. Based on a practical linear tubular magnetic gear, the validity and accuracy of the proposed analytical calculation are well verified by

comparing the calculation results with that obtained from using the FEM.

ACKNOWLEDGMENT

This work was supported by a grant (Project No. HKU710711E) from the Hong Kong Research Grants Council, Hong Kong Special Administrative Region, China.

APPENDIX A.

Let

$$E(f_1, f_2, r, n) = \frac{I_n(f_1 r)}{I_n(f_2 r)}$$

$$F(f_1, f_2, r, n) = \frac{K_n(f_1 r)}{I_n(f_2 r)}$$

$$G(f_1, f_2, r, n) = \frac{K_n(f_1 r)}{K_n(f_2 r)}$$

$$H(f_1, f_2, r, n) = \frac{I_n(f_1 r)}{K_n(f_2 r)}$$

$$c_0 = \frac{\mu_0}{\sqrt{\mu_{fm\_r}\mu_{fm\_z}}}$$

$$S = \frac{\left[\begin{array}{l} G(\omega_n, p_n, r_{fo}, 0) - c_0 G(\omega_n, p_n, r_{fo}, 1) \\ -F(\omega_n, \omega_n, r_o, 0)\,\lfloor H(\omega_n, p_n, r_{fo}, 0) + c_0 H(\omega_n, p_n, r_{fo}, 1)\rfloor \end{array}\right]}{H(p_n, p_n, r_{fo}, 0) + H(p_n, p_n, r_{fo}, 1)}$$

$$T = \frac{\left[\begin{array}{l} F(\omega_n, p_n, r_{fo}, 0) + c_0 F(\omega_n, p_n, r_{fo}, 1) \\ -F(\omega_n, \omega_n, r_o, 0)\,\lfloor E(\omega_n, p_n, r_{fo}, 0) - c_0 E(\omega_n, p_n, r_{fo}, 1)\rfloor \end{array}\right]}{F(p_n, p_n, r_{fo}, 0) + F(p_n, p_n, r_{fo}, 1)}$$

$$U = \frac{\left[\begin{array}{l} S\,\lfloor c_0 H(p_n, \omega_n, r_{fi}, 0) + H(p_n, \omega_n, r_{fi}, 1)\rfloor \\ +T\,\lfloor c_0 G(p_n, \omega_n, r_{fi}, 0) - G(p_n, \omega_n, r_{fi}, 1)\rfloor \end{array}\right]}{c_0\left[H(\omega_n, \omega_n, r_{fi}, 0) + H(\omega_n, \omega_n, r_{fi}, 1)\right]}$$

$$V = \frac{\left[\begin{array}{l} S\,\lfloor c_0 E(p_n, \omega_n, r_{fi}, 0) - E(p_n, \omega_n, r_{fi}, 1)\rfloor \\ +T\,\lfloor c_0 F(p_n, \omega_n, r_{fi}, 0) + F(p_n, \omega_n, r_{fi}, 1)\rfloor \end{array}\right]}{c_0\left[F(\omega_n, \omega_n, r_{fi}, 0) + F(\omega_n, \omega_n, r_{fi}, 1)\right]}$$

$$W = \frac{U\left[\mu_{rm}H(\omega_n,\omega_n,r_m,0)+H(\omega_n,\omega_n,r_m,1)\right]+V\left(\mu_{rm}-1\right)}{\mu_{rm}\left[H(\omega_n,\omega_n,r_m,0)+H(\omega_n,\omega_n,r_m,1)\right]}$$

$$X = \frac{U\left(\mu_{rm}-1\right)+V\left[\mu_{rm}F(\omega_n,\omega_n,r_m,0)+F(\omega_n,\omega_n,r_m,1)\right]}{\mu_{rm}\left[F(\omega_n,\omega_n,r_m,0)+F(\omega_n,\omega_n,r_m,1)\right]}$$

$$a_n^{IV} = -F(\omega_n,\omega_n,r_o,0)$$

Then, it yields:

$$\begin{aligned}
B_n^{\mathrm{IV}} &= \frac{2R_0M_n}{\left[W+XF(\omega_n,\omega_n,r_i,0)\right]I_0(\omega_n r_i)\omega_n^2} \\
&\quad -\frac{2R_0M_n}{\left[\begin{array}{l}\omega_n^2K_0(\omega_n r_m)\left[H(\omega_n,\omega_n,r_m,0)+H(\omega_n,\omega_n,r_m,1)\right]\\ \left[W+XF(\omega_n,\omega_n,r_i,0)\right]\end{array}\right]} \\
&\quad +\frac{M_n}{\left[\begin{array}{l}\mu_{rm}\omega_nK_1(\omega_n r_m)\left[H(\omega_n,\omega_n,r_m,0)+H(\omega_n,\omega_n,r_m,1)\right]\\ \left[W+XF(\omega_n,\omega_n,r_i,0)\right]\end{array}\right]} \\
&\quad -\frac{2R_0M_nF(\omega_n,\omega_n,r_i,0)}{\left[\begin{array}{l}\omega_n^2I_0(\omega_n r_m)\left[F(\omega_n,\omega_n,r_m,0)+F(\omega_n,\omega_n,r_m,1)\right]\\ \left[W+XF(\omega_n,\omega_n,r_i,0)\right]\end{array}\right]} \\
&\quad -\frac{M_nF(\omega_n,\omega_n,r_i,0)}{\left[\begin{array}{l}\mu_{rm}\omega_nI_1(\omega_n r_m)\left[F(\omega_n,\omega_n,r_m,0)+F(\omega_n,\omega_n,r_m,1)\right]\\ \left[W+XF(\omega_n,\omega_n,r_i,0)\right]\end{array}\right]} \\
A_n^{\mathrm{IV}} &= a_n^{\mathrm{IV}}B_n^{\mathrm{IV}} \\
A_n^{\mathrm{III}} &= SB_n^{\mathrm{IV}} \\
B_n^{\mathrm{III}} &= TB_n^{\mathrm{IV}} \\
A_n^{\mathrm{II}} &= UB_n^{\mathrm{IV}} \\
B_n^{\mathrm{II}} &= VB_n^{\mathrm{IV}} \\
A_n^{\mathrm{I}} &= WB_n^{\mathrm{IV}} + \frac{2R_0M_n}{\omega_n^2K_0(\omega_n r_m)\left[H(\omega_n,\omega_n,r_m,0)+H(\omega_n,\omega_n,r_m,1)\right]} \\
&\quad -\frac{M_n}{\mu_{rm}\omega_nK_1(\omega_n r_m)\left[H(\omega_n,\omega_n,r_m,0)+H(\omega_n,\omega_n,r_m,1)\right]} \\
B_n^{\mathrm{I}} &= XB_n^{\mathrm{IV}} + \frac{2R_0M_n}{\omega_n^2I_0(\omega_n r_m)\left[F(\omega_n,\omega_n,r_m,0)+F(\omega_n,\omega_n,r_m,1)\right]} \\
&\quad +\frac{M_n}{\mu_{rm}\omega_nI_1(\omega_n r_m)\left[F(\omega_n,\omega_n,r_m,0)+F(\omega_n,\omega_n,r_m,1)\right]}
\end{aligned}$$

REFERENCES

1. Liu, X., K. T. Chau, J. Z. Jiang, and C. Yu, "Design and analysis of interior-magnet outer-rotor concentric magnetic gears," *Journal of Applied Physics*, Vol. 105, No. 7, 07F101–07F101-3, 2009.
2. Jian, L., K. T. Chau, Y. Gong, J. Z. Jiang, C. Yu, and W. Li, "Comparison of coaxial magnetic gears with different topologies," *IEEE Transactions on Magnetics*, Vol. 45, No. 10, 4526–4529, 2009.
3. Chau, K. T., D. Zhang, J. Z. Jiang, C. Liu, and Y. J. Zhang, "Design of a magnetic-geared outer-rotor permanent-magnet brushless motor for electric vehicles," *IEEE Transactions on Magnetics*, Vol. 43, No. 6, 2504–2506, 2007.
4. Jian, L. and K.-T. Chau, "Design and analysis of a magnetic-geared electronic-continuously variable transmission system using finite element method," *Progress In Electromagnetics Research*, Vol. 107, 47–61, 2010.
5. Atallah, K., J. Wang, and D. Howe, "A high-performance linear magnetic gear," *Journal of Applied Physics*, Vol. 97, No. 10, 10N516–10N516-3, 2005.
6. Holehouse, R. C., K. Atallah, and J. Wang, "Design and realization of a linear magnetic gear," *IEEE Transactions on Magnetics*, Vol. 47, No. 10, 4171–4174, 2011.
7. Li, W. and K. T. Chau, "A linear magnetic-geared free-piston generator for range-extended electric vehicles," *Journal of Asian Electric Vehicles*, Vol. 8, No. 1, 1345–1350, 2010.
8. Li, W., K. T. Chau, and J. Z. Jiang, "Application of linear magnetic gears for pseudo-direct-drive oceanic wave energy harvesting," *IEEE Transactions on Magnetics*, Vol. 47, No. 10, 2624–2627, 2011.
9. Chau, K. T., D. Zhang, J. Z. Jiang, and L. Jian, "Transient analysis of coaxial magnetic gears using finite element comodeling," *Journal of Applied Physics*, Vol. 103, No. 7, 07F101–07F101-3, 2008.
10. Touati, S., R. Ibtiouen, O. Touhami, and A. Djerdir, "Experimental investigation and optimization of permanent magnet motor based on coupling boundary element method with permeances network," *Progress In Electromagnetics Research*, Vol. 111, 71–90, 2011.
11. Zhang, Y., K. T. Chau, J. Z. Jiang, D. Zhang, and C. Liu, "A finite element — Analytical method for electromagnetic field analysis of electric machines with free rotation," *IEEE Transactions on*

Magnetics, Vol. 42, No. 10, 3392–3394, 2006.

12. Jian, L. and K.-T. Chau, "Analytical calculation of magnetic field distribution in coaxial magnetic gears," *Progress In Electromagnetics Research*, Vol. 92, 1–16, 2009.
13. Gysen, B. L. J., E. A. Lomonova, J. J. H. Paulides, and A. J. A. Vandenput, "Analytical and numerical techniques for solving Laplace and Poisson equations in a tubular permanent-magnet actuator: Part I. Semi-analytical framework," *IEEE Transactions on Magnetics*, Vol. 44, No. 7, 1751–1760, 2008.
14. Bianchi, B., "Analytical field computation of a tubular permanent-magnet linear motor," *IEEE Transactions on Magnetics*, Vol. 36, No. 5, 3798–3801, 2000.